Phys. Med. Biol. **44** (1999) 423–440. Printed in the UK PII: S0031-9155(99)97337-2

A sensor-weighted overlapping-sphere head model and exhaustive head model comparison for MEG

M X Huang†‡, J C Mosher§ and R M Leahy‖

† Neuroimaging Center, Building 49 (114M), New Mexico Regional Federal Medical Center, 1501 San Pedro Drive, SE, Albuquerque, NM 87108, USA
‡ Department of Radiology, School of Medicine, Health Sciences Center, University of New Mexico, Albuquerque, NM 87131, USA
§ Design Technology, MS-D454, Los Alamos National Laboratory, Los Alamos, NM 87545, USA
‖ Signal and Image Processing Institute, University of Southern California, Los Angeles, CA 90089-2564, USA

Received 9 September 1998

Abstract. The spherical head model has been used in magnetoencephalography (MEG) as a simple forward model for calculating the external magnetic fields resulting from neural activity. For more realistic head shapes, the boundary element method (BEM) or similar numerical methods are used, but at greatly increased computational cost. We introduce a sensor-weighted overlapping-sphere (OS) head model for rapid calculation of more realistic head shapes. The volume currents associated with primary neural activity are used to fit spherical head models for each individual MEG sensor such that the head is more realistically modelled as a set of overlapping spheres, rather than a single sphere. To assist in the evaluation of this OS model with BEM and other head models, we also introduce a novel comparison technique that is based on a generalized eigenvalue decomposition and accounts for the presence of noise in the MEG data. With this technique we can examine the worst possible errors for thousands of dipole locations in a realistic brain volume. We test the traditional single-sphere model, three-shell and single-shell BEM, and the new OS model. The results show that the OS model has accuracy similar to the BEM but is orders of magnitude faster to compute.

1. Introduction

For decades the spherical head model has been used in electroencephalography (EEG) and magnetoencephalography (MEG) as a simple forward model for calculating scalp potentials and external magnetic fields. Compared with numerical techniques for more realistic head shapes, the spherical model is extremely fast to compute. Although empirical evidence suggests that the spherical model is adequate for a number of applications, numerous researchers have studied more realistic alternative models (Meijs *et al* 1987, Hämäläinen and Sarvas 1989, Cuffin 1990, Ferguson *et al* 1994). Typically these models approximate the head as a set of homogeneous layers, each layer separated by boundaries readily extracted from anatomical magnetic resonance (MR) or x-ray computed tomography (CT) images. These surfaces are used in a boundary element method (BEM) to solve the 'forward problem', i.e. to calculate the external magnetic fields for known sources. Typical layers used in such an analysis are the scalp, outer skull surface and inner skull surface. However, the use of BEM methods is limited by their lengthy computation time, as well as huge computer memory requirements for matrix inversion,

0031-9155/99/020423+18$19.50

and the additional complexities of obtaining, storing and extracting the requisite surfaces from anatomical images. Here we introduce the sensor-weighted overlapping-sphere (OS) head model which fits the return currents of a realistic head model with multiple overlapping spheres on a sensor-by-sensor basis. The computational cost of the OS head model is almost the same as that of the single-sphere model. The theoretical foundations of this OS head model are laid out below and its performance compared with those of the single-sphere and BEM models.

A novel error performance measure is also presented to perform an exhaustive head model comparison for MEG. Typically, two MEG head models are compared using a small number of dipole locations and preassigned orientations (Hämäläinen and Sarvas 1989, Schlitt *et al* 1994). Although useful, these comparisons provide information about the model performance in a limited region of the head and only for the preassigned orientations. In this study we introduce a technique based on the generalized eigenvalue decomposition to test thousands of dipole locations efficiently. For each dipole location, the generalized eigenvalue decomposition identifies the dipole orientation in which the two models under comparison differ the most. Simultaneously, the decomposition also identifies the orientation for the minimum difference. This provides a nearly exhaustive comparison so that a complete picture of the relative performance of the head models is obtained.

A widely used metric for the difference between two head models has been the percentage error, also referred to as the relative difference measure and related terms. However, this measure does not address the problem of field values that are too small to be of concern given the anticipated noise power in the measurements. For instance, a very deep source produces a weak external magnetic field so that a small field difference between two head models can yield a very large percentage error. An inverse procedure would not detect this model difference since these weak sensor measurements will be dominated by noise. We therefore 'regularize' the percentage error function to reduce its sensitivity to immeasurable differences and allow a more useful comparison of head models. When combined with the generalized eigenvalue decomposition, this regularized percentage error (RPE) identifies dipole locations and orientations for which the error is substantial compared with expected noise levels.

2. Methods

2.1. Quasistatic electromagnetic surface integrals

A standard approximate model for the head is a set of connected volumes, typically representing the scalp, skull and brain. If the conductivities within each of these regions are isotropic and constant, the electric potentials can be expressed as surface integrals. We assume the head is modelled by a piecewise homogeneous volume conductor G. We denote the surfaces between compartments with different conductivity as $S_1, S_2, \ldots, S_m$. Under the quasistatic approximation, the electric potential $V(\boldsymbol{r})$ on the jth surface can be expressed by the Fredholm integral of the second kind (Geselowitz 1970):

$$V(\boldsymbol{r}) = \frac{2\sigma_m}{\sigma_i^- + \sigma_i^+} V_\infty(\boldsymbol{r}) - \frac{1}{2\pi} \sum_{i=1}^{m} \frac{\sigma_i^- - \sigma_i^+}{\sigma_i^- + \sigma_i^+} \int_{S_i} V(\boldsymbol{r}') \boldsymbol{n}(\boldsymbol{r}') \cdot \frac{\boldsymbol{r} - \boldsymbol{r}'}{\|\boldsymbol{r} - \boldsymbol{r}'\|^3} \, \mathrm{d}s_i' \qquad \boldsymbol{r} \in S_i \tag{1}$$

where $V_\infty(\boldsymbol{r})$ is the electric potential in an infinite homogeneous medium

$$V_\infty(\boldsymbol{r}) = \frac{1}{4\pi\sigma_m} \int_G \boldsymbol{j}^p(\boldsymbol{r}') \cdot \frac{\boldsymbol{r} - \boldsymbol{r}'}{\|\boldsymbol{r} - \boldsymbol{r}'\|^3} \, \mathrm{d}v' \tag{2}$$

σ_i^- and σ_i^+ are the conductivities inside and outside the jth surface, $\boldsymbol{n}(\boldsymbol{r}')\,\mathrm{d}s_i'$ is a vector element of surface S_i oriented along the outward unit norm of S_i, and $\boldsymbol{j}^p(\boldsymbol{r}')$ is the primary current. Once the potential $V(\boldsymbol{r})$ is obtained on all surfaces, the magnetic field can be computed as (Geselowitz 1967, 1970)

$$\boldsymbol{B}(\boldsymbol{r}) = \boldsymbol{B}_\infty(\boldsymbol{r}) - \frac{\mu_0}{4\pi}\sum_{i=1}^{m}(\sigma_i^- - \sigma_i^+)\int_{S_i} V(\boldsymbol{r}')\boldsymbol{n}(\boldsymbol{r}')\times\frac{\boldsymbol{r}-\boldsymbol{r}'}{\|\boldsymbol{r}-\boldsymbol{r}'\|^3}\,\mathrm{d}s_i' \tag{3}$$

where the corresponding magnetic field in an infinite homogeneous medium is

$$\boldsymbol{B}_\infty(\boldsymbol{r}) = \frac{\mu_0}{4\pi}\int_G \boldsymbol{j}^p(\boldsymbol{r}')\times\frac{\boldsymbol{r}-\boldsymbol{r}'}{\|\boldsymbol{r}-\boldsymbol{r}'\|^3}\,\mathrm{d}v'. \tag{4}$$

$\boldsymbol{B}_\infty(\boldsymbol{r})$ is only related to the primary current and is therefore independent of the head geometry. The second terms on the right-hand side of (1) and (3) represent the return currents which arise from the 'fictitious' or 'secondary' current distribution $\boldsymbol{j}^f(\boldsymbol{r}') = -(\sigma_i^- - \sigma_i^+)V(\boldsymbol{r}')\boldsymbol{n}(\boldsymbol{r}') = j^f(\boldsymbol{r}')\boldsymbol{n}(\boldsymbol{r}')$ on each surface.

For general surface shapes, analytical solutions to (1) and (3) are not possible, and numerical solutions such as the boundary element method (BEM) have to be pursued. Using anatomical MR or x-ray CT images, the surfaces are identified, tessellated with small-area elements, and conductivities assigned to each volume. In this study the ratio of conductivities of scalp:skull:brain was chosen to be 100:1:100. We refer to this model as a three-shell BEM model and consider it to be the standard against which we compare other models.

As reviewed in Mosher *et al* (1999), several methods have been proposed to solve the boundary element equations. In this study the 'linear collocation' method (Schlitt *et al* 1994) was adopted for solving for the electric potentials, then the formula of Ferguson *et al* (1994) was used for calculating the integral in equation (3) to obtain the magnetic fields. Calculating the three-shell BEM model can be computationally intensive. Noting that the total surface integral in (3) results mainly from the contribution of the inner skull surface (due to the relatively low skull conductivity), Hämäläinen and Sarvas (1989) suggest a single-shell BEM comprising just the innermost surface. They present a comparison with the three-shell BEM for about 20–30 dipole locations and preassigned orientations. In section 3 we extend this comparison to thousands of dipole locations and test for the worst possible error over all possible dipole orientations.

If the conducting body comprises concentric spheres, Sarvas (1987) has shown that (3) can be expressed in closed form for a current dipole source inside the sphere. Traditionally, as an approximation to the real head, a single sphere which best fits the entire head is widely used in MEG forward calculations. This model is approximately three orders of magnitude faster to compute than the BEM models. In addition, unlike the BEM, no conductivity profile is explicitly required in the calculation using the spherical head model. However, although it has been widely applied, this single sphere head model has been criticized as inadequate for some regions, for example frontal and frontal-temporal areas (Hämäläinen and Sarvas 1989). The OS model described below attempts to retain the computational efficiency of the spherical model while achieving accuracy close to that of the BEM.

2.2. Interpolating the BEM with overlapping spheres

The forward problem must often be solved for thousands of possible source configurations when solving the inverse problem. Evaluating the BEM forward model can be computationally infeasible in inverse algorithms that adjust multiple dipole locations in order to minimize a cost function. One approach to avoiding BEM calculations during the inverse fitting is to preselect a grid of dipole locations and calculate the forward model only at those locations

(Huang *et al* 1998). The forward field for an arbitrary point within the head is then found by interpolating the forward model from nearby grid points.

The forward problem for the sphere is markedly simpler than the BEM, and a natural extension of the single-sphere model is to use multiple spheres. One can imagine that the best fitting sphere for the occipital region of the brain will be different from the best fitting sphere for the frontal region, as suggested for instance in the figure of Ilmoniemi *et al* (1985) showing two such locally fitted spheres. Here, rather than find a single locally best fitting sphere for all sensors based on the head geometry, we instead fit the spherical model on a sensor-by-sensor basis using a set of grid points within the brain. The centre of the sphere for each sensor is chosen to minimize the error with respect to the field calculated using the three-shell BEM over the entire set of grid points. The forward model for an arbitrary dipole point is then solved using the simpler sphere solution assigned to that sensor.

The procedure is the following: (i) for a single MEG sensor, we first calculate the lead field over thousands of dipole locations using the three-shell BEM model; (ii) make an initial guess of the best fitting sphere centre (for example the best fitting sphere centre for the entire head), and calculate the lead field using the Sarvas formula over the same set of dipole locations; (iii) calculate the cross-correlation between these above two lead fields; (iv) adjust the centre of the sphere and repeat (ii) and (iii) until the highest cross-correlation is achieved. The result is a best-fitting sphere for each sensor, yielding a set of overlapping spheres spanning the realistic head shape as schematically represented in figure 1. This OS model can be effectively used as the interpolating function for the forward solution generated over the grid of points using the BEM. The principal drawback of this approach is the need to calculate the BEM solution first in order to obtain the overlapping spheres.

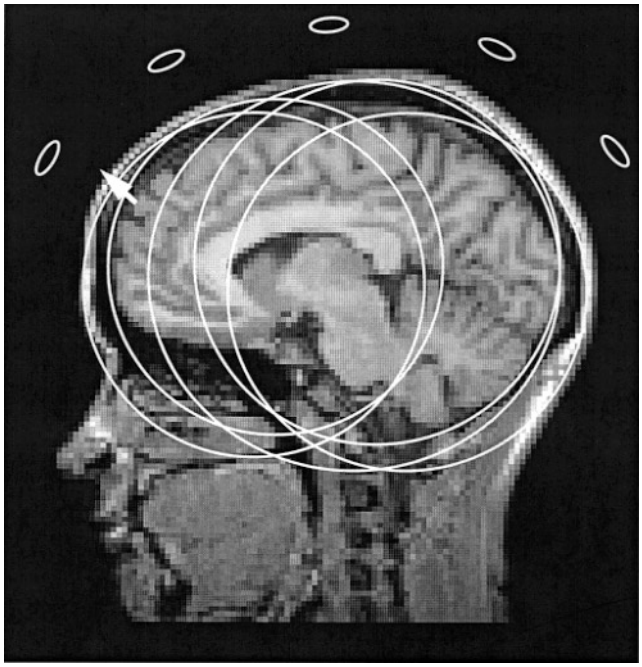

Figure 1. A schematic plot of the sensor-weighted overlapping-sphere model. The arrow represents the location and radial orientation of a dipole that was used in our case study.

2.3. Overlapping spheres without the BEM

To solve the forward problem without resorting to a BEM, one can fit a sphere to the local curvature of the skull in the vicinity of the sensor. Although this approach is quite intuitive, the difficulty lies in rigorously deciding how much of the skull is 'local' to a sensor. At one extreme, we can define a tiny area on the head just under the MEG sensor to be local. At the other, we can treat the entire skull as local, which reduces to the traditional single-sphere model.

We propose a method to obtain the overlapping spheres by fitting the return current contribution term in (3) using a spherical model. For a given MEG sensor at location $\boldsymbol{r}$ with orientation $\boldsymbol{o}$, we require

$$\sum_{i=1}^{m} \int_{S_i^{\mathrm{re}}} \left[\left(\boldsymbol{o}(\boldsymbol{r}) \cdot \boldsymbol{n}^{\mathrm{re}}(\boldsymbol{r}') \times \frac{\boldsymbol{r} - \boldsymbol{r}'_{\mathrm{re}}}{\|\boldsymbol{r} - \boldsymbol{r}'_{\mathrm{re}}\|^3} \right) j^f_{\mathrm{re}}(\boldsymbol{r}') \, \mathrm{d}s'_i \right.$$
$$\left. - \int_{S_i^{\mathrm{sp}}} \left(\boldsymbol{o}(\boldsymbol{r}) \cdot \boldsymbol{n}^{\mathrm{sp}}(\boldsymbol{r}') \times \frac{\boldsymbol{r} - \boldsymbol{r}'_{\mathrm{sp}}}{\|\boldsymbol{r} - \boldsymbol{r}'_{\mathrm{sp}}\|^3} \right) j^f_{\mathrm{sp}}(\boldsymbol{r}') \, \mathrm{d}s'_i \right] \simeq 0 \tag{5}$$

where the superscripts 're' and 'sp' stand for the realistic head and its spherical approximation respectively. In other words, we seek a spherical model whose secondary currents are effectively identical to those of the true surface model. We approach this solution by making some simplifying assumptions.

The conductivity of the human skull is about two orders of magnitude less than the conductivities of the other compartments (for example scalp and brain), and the dominant return current contributions will come from the innermost skull. Therefore, a good approximation is to assume the skull is totally insulated (Hämäläinen and Sarvas 1989). Using this 'isolated skull approach', we can evaluate the integral on the innermost skull surface only, thus reducing the complexity of the calculation in (5). The historical utility of the spherical model indicates that the true potentials are not dramatically different from the spherical potentials, and we therefore do not expect major differences between j^f_{re} and j^f_{sp}. With these approximations in mind, we can rewrite equation (5) as

$$\int_{S^{\mathrm{re}}_{\mathrm{innerskull}}} \left(\boldsymbol{o}(\boldsymbol{r}) \cdot \boldsymbol{n}^{\mathrm{re}}(\boldsymbol{r}') \times \frac{\boldsymbol{r} - \boldsymbol{r}'_{\mathrm{re}}}{\|\boldsymbol{r} - \boldsymbol{r}'_{\mathrm{re}}\|^3} - \boldsymbol{o}(\boldsymbol{r}) \cdot \boldsymbol{n}^{\mathrm{sp}}(\boldsymbol{r}') \times \frac{\boldsymbol{r} - \boldsymbol{r}'_{\mathrm{sp}}}{\|\boldsymbol{r} - \boldsymbol{r}'_{\mathrm{sp}}\|^3} \right) j^f_{\mathrm{re}}(\boldsymbol{r}') \, \mathrm{d}s' \simeq 0. \tag{6}$$

To solve this numerically we use a dense surface mesh containing N points to represent the realistic innermost skull surface, and the same number of points for the fitting sphere. The least-squares fitting problem is simply to minimize the cost function:

$$\sum_{i=1}^{N} \left\| \boldsymbol{o} \cdot \boldsymbol{n}^{\mathrm{re}}(i) \times \frac{\boldsymbol{r} - \boldsymbol{r}'_{\mathrm{re}}(i)}{\|\boldsymbol{r} - \boldsymbol{r}'_{\mathrm{re}}(i)\|^3} - \boldsymbol{o} \cdot \boldsymbol{n}^{\mathrm{sp}}(i) \times \frac{\boldsymbol{r} - \boldsymbol{r}'_{\mathrm{sp}}(i)}{\|\boldsymbol{r} - \boldsymbol{r}'_{\mathrm{sp}}(i)\|^3} \right\|^2 \tag{7}$$

where $\boldsymbol{r}'_{\mathrm{re}}(i)$ and $\boldsymbol{n}^{\mathrm{re}}(i)$ are, respectively, the locations and normal orientations of the mesh points on the innermost skull surface; $\boldsymbol{r}'_{\mathrm{sp}}(i)$ and $\boldsymbol{n}^{\mathrm{sp}}(i)$ are the corresponding parameters of the mesh points on the approximating sphere. For a given centre and radius of the sphere, $\boldsymbol{r}'_{\mathrm{sp}}(i)$ is obtained by radially mapping $\boldsymbol{r}'_{\mathrm{re}}(i)$ to the surface of the sphere. If we designate $\boldsymbol{C}_0$ to represent the centre of the fitting sphere and R_0 the sphere's radius, we can substitute expressions for the spherical parameters in terms of the true surface parameters as

$$\boldsymbol{n}^{\mathrm{sp}}(i) = (\boldsymbol{r}'_{\mathrm{re}}(i) - \boldsymbol{C}_0)/\|\boldsymbol{r}'_{\mathrm{re}}(i) - \boldsymbol{C}_0\| \tag{8}$$

and

$$\boldsymbol{r}'_{\mathrm{sp}}(i) = R_0[(\boldsymbol{r}'_{\mathrm{re}}(i) - \boldsymbol{C}_0)/\|\boldsymbol{r}'_{\mathrm{re}}(i) - \boldsymbol{C}_0\|] + \boldsymbol{C}_0. \tag{9}$$

Therefore, (7) can be rewritten as

$$\sum_{i=1}^{N} \left\| \boldsymbol{o}\cdot\boldsymbol{n}^{\mathrm{re}}(i) \times \frac{\boldsymbol{r}-\boldsymbol{r}'_{\mathrm{re}}(i)}{\|\boldsymbol{r}-\boldsymbol{r}'_{\mathrm{re}}(i)\|^3} - \boldsymbol{o}\cdot\frac{\boldsymbol{r}'_{\mathrm{re}}(i)-\boldsymbol{C}_0}{\|\boldsymbol{r}'_{\mathrm{re}}(i)-\boldsymbol{C}_0\|} \times \frac{\boldsymbol{r}-\boldsymbol{C}_0}{\|\boldsymbol{r}-R_0((\boldsymbol{r}'_{\mathrm{re}}(i)-\boldsymbol{C}_0)/\|\boldsymbol{r}'_{\mathrm{re}}(i)-\boldsymbol{C}_0\|)-\boldsymbol{C}_0\|^3} \right\|^2. \tag{10}$$

To actually calculate the best fitting sphere for each MEG sensor, we first chose an initial guess of the sphere centre and radius. We then minimize (10) by iteratively adjusting the parameters using the simplex method of Nelder and Mead (1965). The procedure is repeated for each MEG sensor yielding a set of overlapping spheres. Equation (10) is designed for magnetometer sensors. For axial and planar gradiometers that contain multiple coils, one can replace each of the mixed-product terms in (10) with corresponding multiple terms associated with the multiple pick-up coils.

2.4. Regularized percentage error

In order to evaluate the adequacy of the OS and other head models in solving the forward problem, we introduce an error measurement function designed to highlight application of these models to the inverse problem. This function addresses two problems we encounter in comparing head models: (1) random noise contaminating the measurements and (2) arbitrary dipole orientations.

We begin with a simple vector example, then progress into the design of the array transfer matrix representing our head model. We assume that the exact head model approach has generated a 'gain matrix' $\mathbf{A}$ for a given MEG sensor array and dipole location. An approximate head model generates a similar gain matrix $\mathbf{B}$ for the same sensor and dipole configurations. For a particular dipole moment $\boldsymbol{q}$, the forward field observed at M sensors is $\boldsymbol{a} = \mathbf{A}\boldsymbol{q}$ or $\boldsymbol{b} = \mathbf{B}\boldsymbol{q}$. Ordinarily we might define the percentage error as

$$\|\boldsymbol{a}-\boldsymbol{b}\|_2^2/\|\boldsymbol{a}\|_2^2 \times 100\% \tag{11}$$

where $\|\cdot\|_2^2$ denotes the square of the l_2 norm of the vector.

This error function (11) and its variations have been widely used by other MEG and EEG researchers in evaluating head models (Meijs *et al* 1987, Hämäläinen and Sarvas 1989, Cuffin 1990, Schlitt *et al* 1995). In each of these instances, the error was scaled by the field value in order to achieve a figure of merit. A problem arises when the field values are too small to be of concern. For example, a radial dipole inside a perfect sphere has zero external magnetic field, and in a realistic head shape the external field can be expected to be quite small. In these instances, the error measures above will yield widely varying figures of merit for different forward models, yet in the inverse problem these small field differences will almost surely be dominated by noise at the sensors.

In this study we modify the existing error function (11) to account for an anticipated noise variance. Suppose that the true measurement $\boldsymbol{a}$ is corrupted by a random noise vector $\boldsymbol{n}$ so that the expected squared norm of the noisy measurement is $\|\boldsymbol{a}\|_2^2 + M\sigma^2$, i.e. $\boldsymbol{n}$ comprises M i.i.d. elements of zero mean and σ^2 variance. In this case, a more appropriate measure of the normalized error in the data between the true and approximate forward models should include the noise power as part of the normalization, i.e. we define the *regularized percentage error* (RPE) due to the model mismatch as

$$\frac{\|\boldsymbol{a}-\boldsymbol{b}\|_2^2}{\|\boldsymbol{a}\|_2^2 + M\sigma^2} \times 100\% = \frac{\|\boldsymbol{a}-\boldsymbol{b}\|_2^2}{\|\boldsymbol{a}\|_2^2[1 + M(\sigma^2/\|\boldsymbol{a}\|_2^2)]} \times 100\%. \tag{12}$$

In other words, by normalizing the error by the expected squared norm of the noisy model, the percentage error is less sensitive to small errors for sources that produce small signal power.

The difference between PE and RPE can be found in figure 2, for a typical noise level for averaged MEG data of 10 fT, for one MEG sensor, i.e. $M = 1$. The full curves are the RPEs as functions of the field strength, $\sqrt{\|\boldsymbol{a}\|_2^2}$. The broken curves are the traditional PE plots. Different levels of errors due to head modelling are plotted. For high field strength, the two sets of curves merge. This is the situation when the first term in the denominator of (12) dominates and the second term is negligible. In this case, (12) is essentially the same as (11). However, for small field strength, significant differences are observed. For example, if the head modelling error is 1 fT, the PE reaches 100% error for a field strength of 1 fT, but the RPE is only about 1% in the same situation. Such a significant difference results from the regularized term that we added in (12). Including the anticipated noise level allows us to properly handle circumstances in which the external fields are very weak.

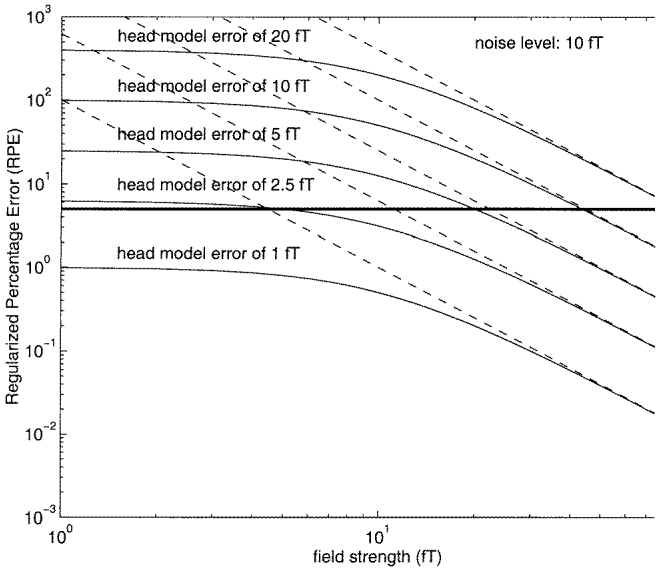

Figure 2. Regularized percentage error versus field strength for a 10 fT noise level and for one MEG sensor. The full curves are the regularized percentage errors as functions of magnetic field strength. Five different model error levels are plotted. The corresponding broken curves are the traditional percentage error. The thick horizontal line represents the 5% error line.

We would also like to relax the requirement of specifying the dipole moment, instead maximizing or minimizing the error over all possible dipole orientations. In this case we retain the dipole moment $\boldsymbol{q}$ in the expression for the percentage error:

$$\frac{\|(\mathbf{A}-\mathbf{B})\boldsymbol{q}\|_2^2}{\|\mathbf{A}\boldsymbol{q}\|_2^2} \times 100\%. \tag{13}$$

To evaluate (13) we need to specify the dipole moment $\boldsymbol{q}$. Rather than evaluate this function for a particular orientation we can instead find the orientation, at a particular dipole location,

for which this error is maximum, i.e.

$$\max_{q} \frac{q^T(\mathbf{A}-\mathbf{B})^T(\mathbf{A}-\mathbf{B})q}{q^T\mathbf{A}^T\mathbf{A}q}. \tag{14}$$

The solution to this is well known and found as the maximum of the eigenvalues λ of the generalized eigenvalue problem (Golub and Van Loan 1984):

$$(\mathbf{A}-\mathbf{B})^T(\mathbf{A}-\mathbf{B})q = \lambda\mathbf{A}^T\mathbf{A}q \tag{15}$$

where q is the corresponding generalized eigenvector. The maximum generalized eigenvalue (times 100%) is the maximum percentage error when the moment is oriented in the direction of the corresponding eigenvector. Correspondingly, the minimum eigenvalue is equivalent to the minimum percentage error when the dipole is oriented in the direction of its corresponding eigenvector. All other dipole orientations are bounded by these two values.

Problems with this measure will arise, however, when the model matrix $\mathbf{A}$ has a null space or a weak component. In these instances, particular orientations of q will yield measurement vectors a with a very small norm, or indeed zero norm. A classic example, as we mentioned before, is a radially oriented dipole inside a set of concentric spheres, which generates no external magnetic field. In more realistic head shapes, similarly oriented dipoles yield only weak external fields. In the inverse problem, these weak fields will be dominated by noise, and our error measure should reflect this reality. Analogous to the above vector discussion, we define the RPE as

$$\frac{q^T(\mathbf{A}-\mathbf{B})^T(\mathbf{A}-\mathbf{B})q}{q^T\mathbf{A}^T\mathbf{A}q + M\sigma^2} \times 100\% \tag{16}$$

and find the orientation which gives the maximum RPE as

$$\max_{q} \frac{q^T(\mathbf{A}-\mathbf{B})^T(\mathbf{A}-\mathbf{B})q}{q^T\mathbf{A}^T\mathbf{A}q + M\sigma^2}. \tag{17}$$

Let q denote the norm of q and note that $q^T[\mathbf{A}^T\mathbf{A} + (M\sigma^2/q^2)\mathbf{I}]q = q^T\mathbf{A}^T\mathbf{A}q + M\sigma^2$. We can then rewrite (17) as

$$\max_{q} \frac{q^T(\mathbf{A}-\mathbf{B})^T(\mathbf{A}-\mathbf{B})q}{q^T[\mathbf{A}^T\mathbf{A} + (M\sigma^2/q^2)\mathbf{I}]q} \tag{18}$$

where we define the quantity q^2/σ^2 to be the signal-to-noise ratio (SNR). Again the solution is found as the maximum eigenvalue of the generalized eigenvalue problem:

$$(\mathbf{A}-\mathbf{B})^T(\mathbf{A}-\mathbf{B})q = \lambda[\mathbf{A}^T\mathbf{A} + (M\sigma^2/q^2)\mathbf{I}]q. \tag{19}$$

This *constrained maximized regularized percentage error* assumes that the dipole moment q is exactly the same in both models. However, in practice we often find the numerical models introduce small errors that effectively alter the dipole magnitude or orientation. This is particularly true in MEG for radially oriented dipoles since the forward calculations involve a cancelling operation between the contributions from the primary current and the contributions from the volume currents. In the EEG case, minor differences in the conductivity values or ratios can also lead to relatively inconsequential differences in dipole magnitude, yet again distort the error measure. Differences in tessellation often cause numerical shifting of the dipole orientation when the dipole is close to the inner skull surface (Schlitt *et al* 1994).

We therefore can compare the true and approximate forward models, $\mathbf{A}$ and $\mathbf{B}$, for a particular dipole location, by allowing the moments for the two models to be different. For a

given dipole moment $\boldsymbol{q}$ applied to $\mathbf{A}$, we can find the dipole moment $\tilde{\boldsymbol{q}}$, that when applied to $\mathbf{B}$ produces the minimum squared error $\|\mathbf{A}\boldsymbol{q} - \mathbf{B}\tilde{\boldsymbol{q}}\|^2$, as $\tilde{\boldsymbol{q}} = \mathbf{B}^{\dagger}\mathbf{A}\boldsymbol{q}$, where $\mathbf{B}^{\dagger}$ is the pseudo-inverse of $\mathbf{B}$. Substituting this least squares estimate of the optimal dipole moment $\tilde{\boldsymbol{q}}$ into the RPE expression gives

$$\frac{\|\mathbf{A}\boldsymbol{q} - \mathbf{B}\tilde{\boldsymbol{q}}\|_2^2}{\boldsymbol{q}^T\mathbf{A}^T\mathbf{A}\boldsymbol{q} + M\sigma^2} = \frac{\|\mathbf{A}\boldsymbol{q} - \mathbf{B}\mathbf{B}^{\dagger}\mathbf{A}\boldsymbol{q}\|^2}{\boldsymbol{q}^T\mathbf{A}^T\mathbf{A}\boldsymbol{q} + M\sigma^2} = \frac{\boldsymbol{q}^T\mathbf{A}^T\mathbf{P}_{\mathbf{B}}^{\perp}\mathbf{A}\boldsymbol{q}}{\boldsymbol{q}^T[\mathbf{A}^T\mathbf{A} + (M\sigma^2/q^2)\mathbf{I}]\boldsymbol{q}} \tag{20}$$

where $\mathbf{P}_{\mathbf{B}}^{\perp} = (\mathbf{I} - \mathbf{B}\mathbf{B}^{\dagger})$. The maximum value of the *unconstrained maximized regularized percentage error* is then found as the maximum of (20), or equivalently the maximum eigenvalue of the generalized eigenvalue problem:

$$\mathbf{A}^T\mathbf{P}_{\mathbf{B}}^{\perp}\mathbf{A}\boldsymbol{q} = \lambda[\mathbf{A}^T\mathbf{A} + (M\sigma^2/q^2)\mathbf{I}]\boldsymbol{q} \tag{21}$$

where the moment is the corresponding eigenvector. It is this final form of the *unconstrained maximized regularized percentage error* that we use to perform the exhaustive comparisons below, i.e. we solve (21) at a large number of dipole locations for the maximum RPE and the corresponding dipole orientation.

3. Results

3.1. Simulation set-up

The MEG sensor array that we used in the model comparison contains 127 simulated magnetometers. The 127 sensors are radially oriented and uniformly distributed on an upper hemisphere with 12 cm radius. A human subject's MRI was used as our head volume. The

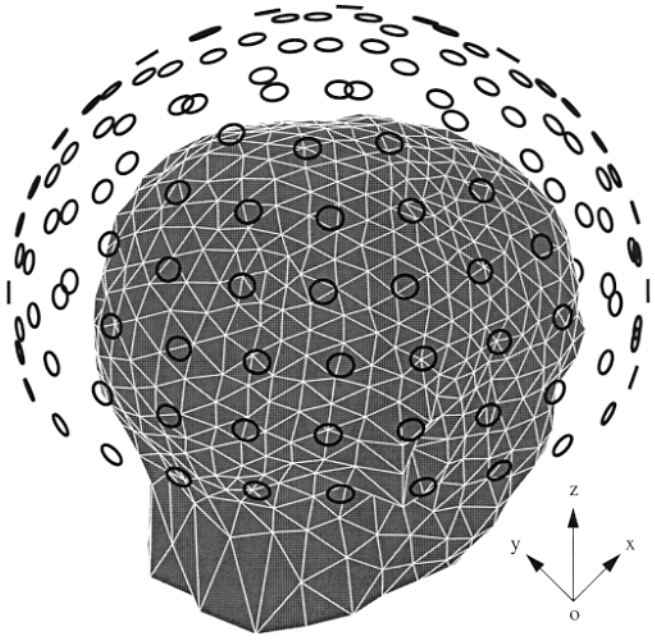

Figure 3. The simulated MEG sensor array and tessellated scalp surface. The 127 radial oriented magnetometers are uniformly distributed on a 12 cm hemisphere. The scalp, outer skull and inner skull surfaces (from an MRI) are each tessellated into 1280 triangles.

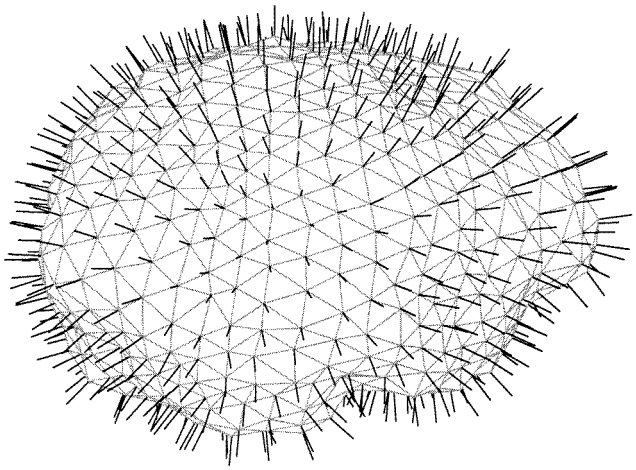

Figure 4. The innermost skull surface of the subject (from MRI) were tessellated into 642 vertices or 1280 triangles. This tessellated mesh was used in our BEM calculations. Also, the vertices (the locations and orientations shown in this figure) were also used as collocation points when forming our sensor-weighted overlapping-sphere model.

surface of the scalp, outer skull and inner skull were extracted from the MRI, and each surface was tessellated into 1280 small triangles using MRIVIEW (Ranken and George 1993), a software package developed in the Biophysics Group at the Los Alamos National Laboratory. Figure 3 shows the 127 simulated MEG sensor with a triangular tessellated scalp surface. The head coordinate system was determined in the following way: the y-axis was chosen to be the line that joins the right and left periauricular (PA) points, with the positive y-axis pointing to the left PA. The origin of this coordinate system was chosen to be the intersection of a line that passed through the nasion and perpendicular to the y-axis. The positive x-axis pointed from the origin to the nasion. Finally, the positive z-axis pointed out through the top of the head, perpendicular to the x–y plane. The tessellated innermost skull surface with the normal orientations of the vertices is shown in figure 4. The tessellated scalp and innermost skull, along with the tessellated outermost skull (not plotted here), were used in our BEM calculations. The locations and orientations of the vertices on the innermost skull were also used to calculate our OS model. In addition, the entire brain volume was divided into a dipole grid containing seven layers of dipoles at different depths for a total of 3294 dipole locations throughout the head volume.

3.2. Dipole case study

Before presenting the RPE over the head volume, we first present a case study of a single dipole, in order to highlight the utilities and differences between the various measures of performance. We selected a dipole in the frontal region of the head (see figure 1), where the single spherical model is often inaccurate. The standard model matrix was computed by the BEM for the MEG array described above. The competing design matrix was computed by the sensor-weighted OS method for the same MEG array. We first computed the percentage error in the three orthogonal dipole directions x, y, z, using (11), as listed in table 1. We then computed the constrained unregularized percentage error using (15) to find the maximum and minimum errors and the corresponding orientations, also listed in table 1.

Table 1. Regularized percentage error.

Technique	Max error (%)	RMS of field (fT)	Orientation	Min error (%)	RMS of field (fT)	Orientation
Cartesian PE	11.24	22.21	[1 0 0]	4.41	31.70	[0 1 0]
Constrained PE (infinite SNR)	51190.2	0.46	[0.73 −0.14 0.67]	1.13	32.70	[0.73 −0.01 −0.69]
Constrained RPE (SNR = 100)	9072.95	0.46	[0.73 −0.14 0.67]	1.13	32.70	[0.73 −0.01 −0.69]
Constrained RPE (SNR = 1)	110.18	0.58	[0.72 −0.15 0.67]	1.03	32.69	[0.73 −0.01 −0.68]
Unconstrained PE (infinite SNR)	79.46	0.47	[0.73 −0.14 0.67]	0.78	7.78	[−0.55 0.11 −0.83]
Unconstrained RPE (SNR = 100)	14.61	0.53	[0.73 −0.14 0.67]	0.76	7.42	[−0.56 0.11 −0.82]
Unconstrained RPE (SNR = 1)	3.41	31.09	[−0.04 0.99 −0.09]	0.11	2.26	[0.68 −0.12 0.72]
			Mislocalization (mm)			
Bias study (noiseless)			4.7 mm (BEM forward, OS inverse)			
Monte Carlo (SNR = 1)			2.5 mm ± 1.1 mm (OS forward and inverse)			
Monte Carlo (SNR = 1)			5.3 mm ± 1.3 mm (BEM forward, OS inverse)			

We assumed an SNR of 1, analogous to a 10 nA m dipole moment in the presence of noise with a 10 fT standard deviation, then recomputed the constrained regularized percentage errors using (19). We also computed the unconstrained unregularized and regularized percentage errors using (21), also listed in table 1. By simply orienting the dipole in the Cartesian directions, we observe a maximum PE of 11% in the x-direction; however, by using the generalized eigenvalue decomposition, we identify a direction in which the two models differ by 51 000%. This dipole orientation corresponds to a nominally radial direction (see figure 1), such that the root-mean-square (RMS) of the external field is quite small, only 0.46 fT for a 10 nA m dipole, as listed in the table. The OS model generates about an 10.6 fT (RMS) field in this exact same orientation and intensity, leading to the large percentage difference. We anticipate, however, that the noise at the sensors will be of 10fT standard deviation, which will dominate sensor measurements, and this PE is unnecessarily magnified. At the same dipole location, if we simply rotate the dipole to a nominally tangential orientation, we see the two models have a PE of about 1%.

In the next row of the table, we regularized the percentage error to 10 fT noise variance, where we now see the dominant error remains nominally in a radial direction. The maximum percentage error is markedly reduced due to the regularizer; the regularizer has virtually no effect on the minimum PE, which represents a substantially stronger signal. When we relax the dipole moment constraint, however, we observe that the errors markedly drop in both noiseless (SNR $= \infty$) and noisy (SNR $= 1$) cases. In the noisy case, the RMS magnetic field strength is 31.09 fT in the worst direction (near y-orientation) calculated by the BEM model, with a percentage error of 3.41%. Thus regularizing the unconstrained percentage error helped identify a dipolar direction for which the error may be considered more substantial in an inverse calculation.

To relate the RPE to dipole localization error, we computed an unconstrained regularized percentage error for an SNR of 1 for this dipole location. We first generated the forward BEM

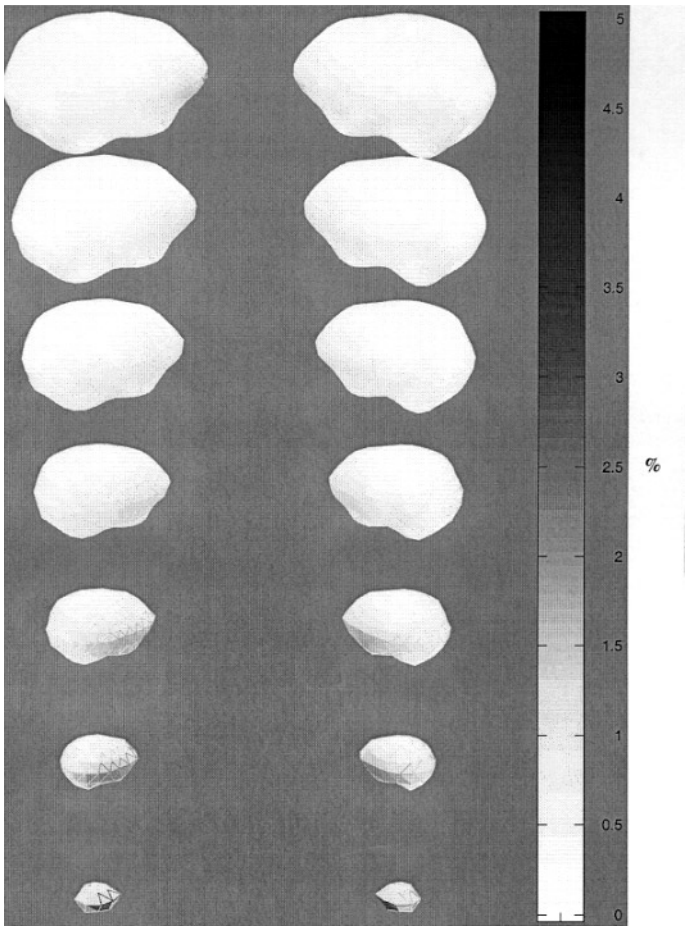

Figure 5. The largest possible unconstrained RPE between single-shell BEM and three-shell BEM assuming an SNR of 1. The analysis was done on a grid containing 3297 dipole locations distributed on seven layers with different depths.

model using the direction identified as having the highest unconstrained RPE. We then used the OS model in an inverse localization. Since no noise was added to the model, the mislocalization gives an indication of the bias that the OS model would inject relative to the BEM model. The mislocalization due to the model error is 4.7 mm, as listed in table 1. Our supposition is that this bias is comparable to the variance that such a localization would encounter in an inverse localization with noise. Using the dipole in this case study, we performed a 200 trial Monte Carlo study, using 10 fT standard deviation noise. The RMS error in the case of the OS model for both forward and inverse is 2.5 mm, versus an RMS error of 5.3 mm for the case of the BEM on the forward and the OS model on the inverse. Although the model bias is somewhat larger than the noise error, this bias was calculated at a location for one of the worst case error differences between the two models; the increase is nonetheless relatively small and acceptable in many inverse studies.

By unconstraining the dipole moment and regularizing the percentage error to account for weak signals, we have identified a dominant dipole direction which yields a 3.4% RPE between the two models. The bias study reveals that the mislocalization of this dipole is relatively small,

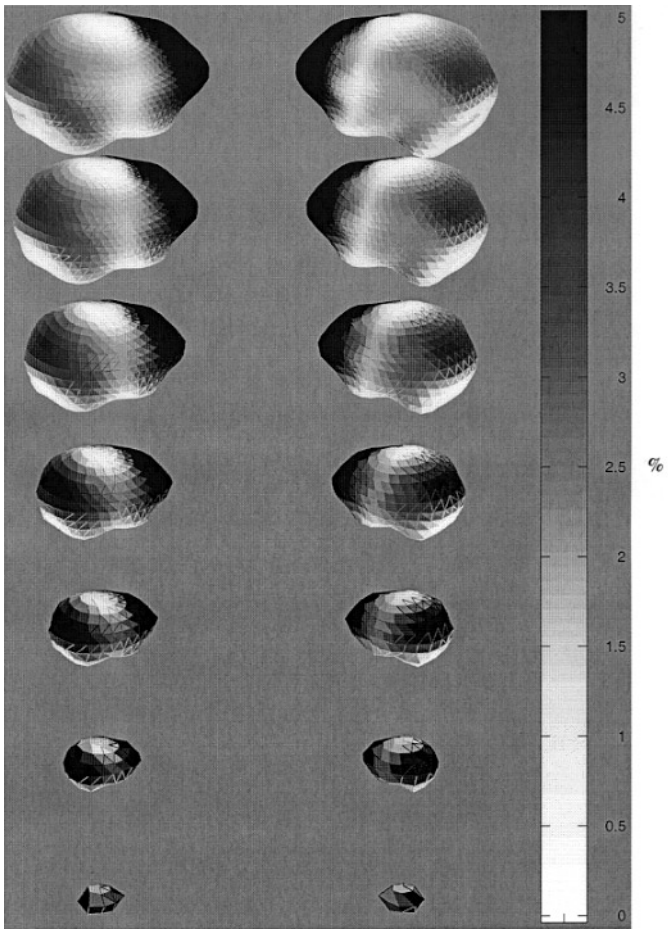

Figure 6. The largest possible unconstrained RPE between the traditional single-sphere model and three-shell BEM.

particularly when we take noise error into account. In the next section, we will examine the model bias throughout the head volume, using the RPE as a guide.

3.3. Exhaustive MEG head model comparisons

We used the unconstrained maximized RPE as a measure to compare several competing head models, including our proposed OS model. The three-shell BEM model was considered the standard against which the other models are compared. We assumed a 10 nA m dipole in the presence of 10 fT standard deviation noise for each MEG channel, for an SNR of 1. The generalized eigenvalue decomposition was applied to obtain the worst possible error for each of the 3294 dipole locations throughout the brain volume.

3.3.1. Single-shell BEM model versus three-shell BEM model. Figure 5 shows the maximum unconstrained RPE for a single-shell BEM assuming the three-shell BEM is the correct model. The figure is scaled such that black indicates an unconstrained RPE of 5% or greater. The unconstrained RPE values are plotted for our dipole grid containing 3294 dipoles on seven

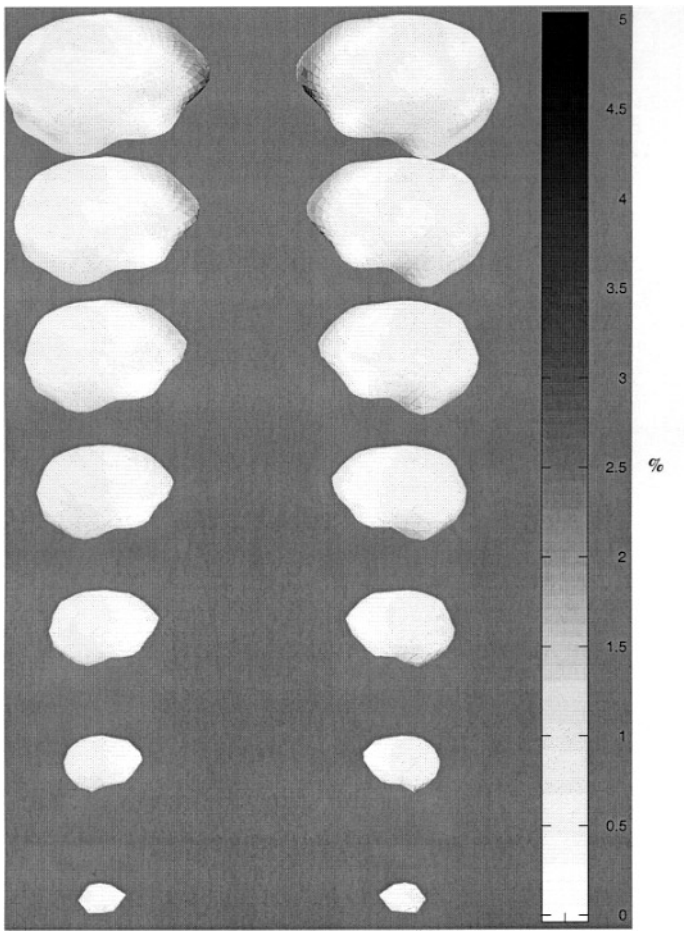

Figure 7. Testing the possibility of matching the performance of three-shell BEM using the sensor-weighted overlapping-sphere model. Again, the largest possible unconstrained RPE is plotted for each dipole.

layers with different depths, and the errors are viewed from two different angles. As one can see from the plot, the unconstrained RPE for almost all the dipole locations is quite small (less than 0.5%). The largest differences observed are about 3% and located in the deep layers of the frontal–temporal regions. The results, in general, agree with those obtained by Hämäläinen and Sarvas (1989), confirming that the single-shell model is a very good approximation to the three-shell model. We also noticed that the deep dipoles in our analysis show less error than was shown by Hämäläinen and Sarvas (1989). This is presumably because we used the RPE instead of the PE, such that the regularization term in (12) has an observable effect on sources that generate weak magnetic fields.

3.3.2. Single-sphere model versus three-shell BEM model. The second comparison is between the traditional single-sphere model and the three-shell BEM. The centre of the sphere is chosen to provide the best least squares fit to the inner skull surface. The largest unconstrained RPE for our seven-layered dipole grid is shown in figure 6. The frontal and frontal–temporal

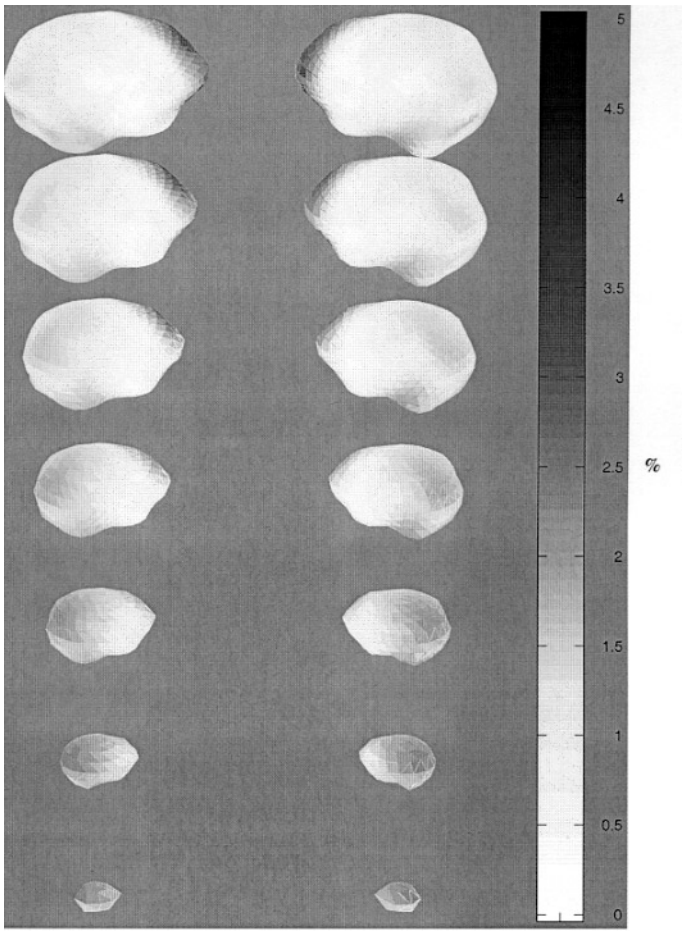

Figure 8. The largest possible unconstrained RPE between the sensor-weighted overlapping-sphere model and the three-shell BEM.

regions show large RPE (>5%). For the occipital and parietal regions, the unconstrained RPE is about 3% for superficial layers and greater for deeper layers. Small errors are observed for the top of the brain and regions along the central sulcus. The results of this comparison have confirmed that for some regions the single-sphere model is indeed overly simplistic.

3.3.3. Interpolated three-shell BEM using the OS model. As we described in section 2, the overlapping spheres are obtained by adjusting their centres so that the discrete lead fields of such a model best match those of the computed three-shell BEM model. Figure 7 shows the maximum unconstrained RPE between these two models. One can see from the plot that for most dipole locations the difference is quite small (less than 0.5%). If we compare this result with the performance of the single-shell BEM (figure 5), we find that they are quite similar. The only exception is for a small portion of the frontal lobe, where the overlapping sphere model gives a somewhat larger error. On the other hand, the OS model outperforms the single-shell BEM for some dipoles on the deeper layers (figure 5). Although the single-shell is faster to compute than the three-shell, we see that the OS model is equivalent in RPE performance at

dramatically lower computational cost. As we mentioned previously, this OS model can be effectively used as the interpolating function for the forward solution generated over the grid of points using BEM. However, this approach requires that we first calculate the BEM model in order to search for the best fitting spheres.

3.3.4. Sensor-weighted OS model versus three-shell BEM model. In section 2 we described the procedure for forming the sensor-weighted OS model without calculating the BEM; rather, we used approximations to the surface integral to fit a sphere on a sensor-by-sensor basis. Figure 8 illustrates the largest unconstrained RPEs for our sensor-weighted OS model relative to the three-shell BEM model. Compared with figure 5 and figure 7, we see comparable RPEs at most locations. Indeed, our case study of the previous section was conducted for one of the larger RPEs of 3.4%. Compared with figure 6 (the single sphere), we see a dramatic improvement in the RPE, yet at virtually no increased computational cost.

For each dipole location in the grid, we used the identified worst case dipole orientation to generate the noiseless forward data for the BEM. We then performed a dipole inverse procedure using the OS model, to record how much bias the OS model introduced relative to the BEM location. In figure 9 we present the model bias for the upper layer of dipoles, as well as RPE for the same locations. We observe that the bias is quite small throughout many regions of the head, consistent with the RPE. For locations near the edge of the array (lower regions of the plot), the bias increases somewhat, approaching 10 mm. In these regions we have the confounding effects of less precision in the BEM (due to neck and facial regions) and decreased sensor coverage, so we remark only that the BEM and OS models begin to

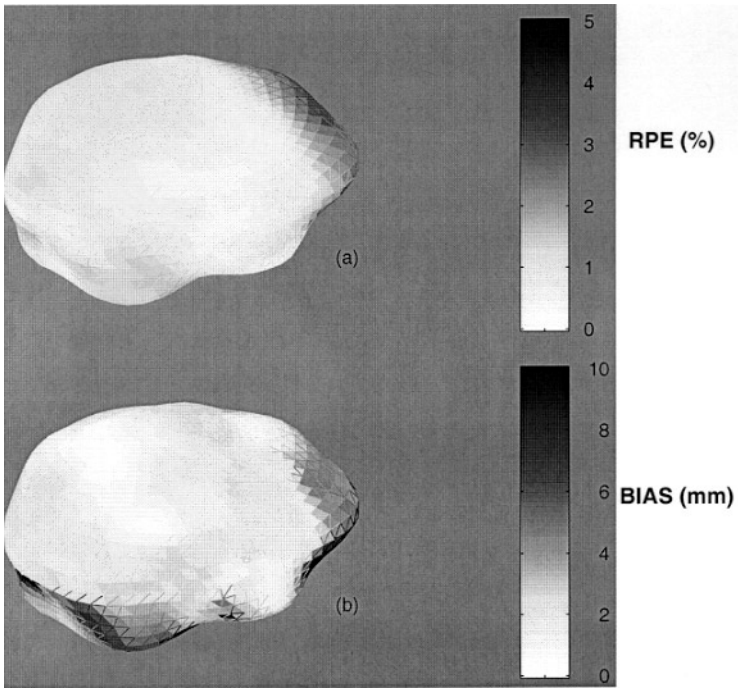

Figure 9. Model bias between the BEM and OS models, using the BEM as the forward model and the OS as the inverse model in an otherwise noiseless inverse procedure. Dipole orientations used were those identified by the RPE as yielding the worst error.

differ in these regions. Throughout much of the upper head the two models are in quite good agreement.

All the calculations presented in this paper were programmed using MATLAB and run on an HP735 workstation with a clock frequency of 125 MHz. Fitting the sphere centres to the MRI for the OS model took about 15 min of computation time. Calculating the OS model for 3294 dipoles and 127 sensor locations required only a few seconds.

4. Discussion

In this paper we have introduced the novel idea of a nearly exhaustive MEG head model comparison using a generalized eigenvalue decomposition. We have applied this technique to a variety of head models and observed that for a small portion of the frontal region, the overlapping-sphere models gave slightly larger differences when compared with the three-shell BEM model (see figure 7 and figure 8). We believe that this is because the head is highly non-spherical in the vicinity of the eye sockets and nasal structures. Although we considered the three-shell BEM to be our 'gold standard', differences between the true conductivities in the head and those assumed in the BEM calculations may in fact introduce larger errors than differences between the BEM and OS models (Leahy *et al* 1998).

It has been noted (Mosher *et al* 1999) that the assumptions made by the BEM can result in significant error under some circumstances. For instance, since finite elements have finite sizes, the forward calculation using the BEM for a source that is quite close to the mesh can have a large error. To avoid this situation in this study, we have purposely designed our dipole grid so that each of the 3294 dipoles was at least 6 mm away from inner skull triangular mesh. However, in reality, the brain activities can sometimes be quite superficial. In order to handle this case, one needs to use very fine meshes (at least in the area of the superficial sources). These finer meshes will no doubt further increase the computational burden and require even larger computer memory for the matrix inversion. On the other hand, the OS model that we have introduced in this paper has no such limitations for superficial sources. Finally, although the sensor-weighted overlapping-sphere head model that we presented in this paper is for MEG, we note that the concept is readily extendable to EEG as well.

5. Conclusions

In this study we have presented a novel technique for MEG head model comparisons using generalized eigenvalue decomposition. This technique automatically computed the smallest and largest possible differences between two head models under comparison. In addition, the traditional error measurement function using percentage error was modified to take into account the anticipated noise level. We applied this method to examine the single-shell BEM model and traditional single-sphere model. The result confirmed that the single-shell BEM model is a very good approximation of the BEM model involving three shells. These results agree with those of Hämäläinen and Sarvas (1989).

The result of the traditional single-sphere model showed that the single sphere is probably too simplistic for some regions of the head. We demonstrated the use of a set of overlapping spheres as a means of interpolating a BEM calculation, negating the need to calculate a full BEM forward model for each iteration in an inverse algorithm. The results showed that this sensor-dependent overlapping-sphere model can have similar accuracy to that of the BEM. We then showed how these spheres could be obtained without the need to calculate the BEM. The centres of the overlapping spheres are fit directly to the skull surface, using a local weighting

function derived from the true surface integral equations. The results showed that this model has similar accuracy to the BEMs for most regions of the brain at greatly reduced computational cost and complexity.

Acknowledgments

This work was supported in part by the National Institute of Mental Health grant R01-MH53213, by National Eye Institute grant R01-EY08610-04, and by Los Alamos National Laboratory, operated by the University of California for the United States Department of Energy under contract W-7405-ENG-36.

References

Cuffin B N 1990 Effects of head shapes on EEGs and MEGs *IEEE Trans. Biomed. Eng.* **37** 15–22

Ferguson A S, Zhang X and Stroink G 1994 A complete linear discretization for calculating the magnetic field using the boundary element method *IEEE Trans. Biomed. Eng.* **41** 455–9

Geselowitz D B 1967 On bioelectric potentials in an inhomogeneous volume conductor *Biophys. J.* **7** 1–11

——1970 On the magnetic field generated outside an inhomogeneous volume conductor by internal volume currents *IEEE Trans. Magn.* **6** 346–7

Golub G H and Van Loan C F 1984 *Matrix Computations* 2nd edn (Baltimore, MD: Johns Hopkins University Press)

Hämäläinen M S and Sarvas J 1989 Realistic conductor geometry model of the human head for interpretation of neuromagnetic data *IEEE Trans. Biomed. Eng.* **36** 165–71

Huang M, Aine C J, Supek S, Best E, Ranken D and Flynn E R 1998 Multi-start downhill simplex method for spatio-temporal source localization in magnetoencephalography *Electroenceph. Clin. Neurophysiol. Evoked Potentials* **108** 32–44

Ilmoniemi R J, Hämäläinen M S and Knuutila J 1985 The forward and inverse problems in the spherical model *Biomagnetism: Applications and Theory* ed H Weinberg, G Stroink and T Katila (New York: Pergamon) pp 278–82

Leahy R M, Mosher J C, Spencer M E, Huang M X and Lewine J D 1998 A study of dipole localization accuracy for MEG and EEG using a human skull phantom *Electroenceph. Clin. Neurophysiol.* **107** 159–73

Meijs J W H, Bosch F G C, Peters M J and Lopes da Silva F H 1987 On the magnetic field distribution generated by a dipolar current source situated in a realistically shaped compartment model of the head *Electroenceph. Clin. Neurophysiol.* **66** 286–98

Mosher J C, Leahy R M and Lewis P S 1999 EEG and MEG: forward solutions for inverse methods *IEEE Trans. Biomed. Eng.* at press

Mosher J C, Lewis P S and Leahy R M 1992 Multiple dipole modeling and localization from spatio-temporal MEG data *IEEE Trans. Biomed. Eng.* **39** 541–57

Mosher J C, Spencer M E, Leahy R M and Lewis P S 1993 Error bounds for EEG and MEG dipole source localization *Electroenceph. Clin. Neurophysiol.* **86** 303–21

Nelder J A and Mead R 1965 A simplex method for function minimization *Comput. J.* **7** 308–13

Ranken D and George J 1993 MRIVIEW: an interactive computational tool for investigation of brain structure and function *Proc. IEEE Visualization '93* (Los Alamitos, CA: IEEE Computer Society Press) pp 324–31

Sarvas J 1987 Basic mathematical and electromagnetic concepts of the bio-magnetic inverse problems *Phys. Med. Biol.* **32** 11–22

Schlitt H, Heller L, Aaron R, Best E and Ranken D 1995 Evaluation of boundary element method for the EEG forward problem: effect of linear interpolation *IEEE Trans. Biomed. Eng.* **42** 52–8

Schlitt H, Heller L, Best E, Ranken D and Aaron R 1994 Effect of conductor geometry on source localization: implications for epilepsy studies *North American Biomagnetism Action Group (Detroit, MI, 15–17 April 1994)* (*Los Alamos Technical Report* LAUR-94-1446)